PAPER • OPEN ACCESS

Evaluating oxide nanoparticle exsolution on A-site deficient $PrBaCo_2O_{6-\delta}$ electrodes

View the article online for updates and enhancements.

Journal of Physics: Energy

OPEN ACCESS

Evaluating oxide nanoparticle exsolution on A-site deficient PrBaCo$_2$O$_{6-\delta}$ electrodes

Alfonso J Carrillo[1] , María Balaguer[1] , Cecilia Solís[2] , Andrés López-García[1] , Sylvio Haas[3], María Fabuel[1], Blanca Delgado-Galicia[1] , Isabelle Rodriguez[1], Einar Vøllestad[4] , Sebastian Wachowski[5] , Ragnar Strandbakke[4,6], Truls Norby[6] and Jose M Serra[1,*]

1 Instituto de Tecnología Química, Universitat Politècnica de València, Consejo Superior de Investigaciones Científicas, 46022 Valencia, Spain
2 German Engineering Materials Science Center (GEMS) at Heinz Maier-Leibnitz Zentrum, Helmholtz-Zentrum Hereon, Lichtenbergstr. 1, 85748 Garching, Germany
3 Deutsches Elektronen Synchrotron (DESY), Notkestr. 85, 22607 Hamburg, Germany
4 Sustainable Energy Technology, SINTEF Industry, Forskningsveien 1, NO-0373 Oslo, Norway
5 Institute of Nanotechnology and Materials Engineering, Faculty of Applied Physics and Mathematics, and Advanced Materials Centre, Gdańsk University of Technology, Gdańsk, Poland
6 Department of Chemistry, University of Oslo, Centre for Materials Science and Nanotechnology, NO-0318 Oslo, Norway
* Author to whom any correspondence should be addressed.

E-mail: jmserra@itq.upv.es

Abstract

Nanoparticle exsolution is a powerful technique for functionalizing redox oxides in energy applications, particularly at high temperatures. It shows promise for solid oxide fuel cells and electrolyzers. However, exsolution of other chemistries like metal oxides is not well studied, and the mechanism is poorly understood. This work explores oxide exsolution in PrBa$_{1-x}$Co$_2$O$_{6-\delta}$ ($x = 0$, 0.05, 0.1, 0.15) double perovskites, practiced electrodes in proton ceramic fuel cells and electrolyzers. Oxide exsolution in PrBa$_{1-x}$Co$_2$O$_{6-\delta}$ aimed at boosting the electrocatalytic activity and was evaluated by varying intrinsic materials-related properties, viz. A-site deficiency and external parameters (temperature, under fixed time, and $pO_2 = 10^{-5}$ atm conditions). The materials were analyzed with conventional characterization tools and synchrotron-based small-angle x-ray scattering. Unlike metal-nanoparticle exsolution, increasing the A-site deficiency did not enhance the extent of oxide-nanoparticle exsolution, whereas larger nanoparticles were obtained by increasing the exsolution temperature. Combined Raman spectroscopy and electron microscopy analysis revealed that BaCoO$_3$, Co$_3$O$_4$, and amorphous BaCO$_3$ nanoparticles were formed on the surface of the double perovskites after the reductive treatments. The present results demonstrate the complexity of oxide-nanoparticle exsolution in comparison with metal-nanoparticle exsolution. Further materials screening and mechanistic studies are needed to enhance our understanding of this method for functionalizing proton ceramic electrochemical cells (PCEC) electrodes.

1. Introduction

Renewable energy storage and conversion are essential for transitioning away from a fossil fuel-based economy. The transformation of renewable electricity into hydrogen via electrolysis is considered one of the main technologies in this sense [1]. Among the different available electrolyzer technologies, proton ceramic electrolyzers (PCEs) stand out due to their higher efficiency [2] and the possibility of working at lower temperatures than solid oxide cells (SOCs). However, the electrolyte resistance and the polarization of the positive electrode (positrode) limit the overall efficiency of these devices. We need positrode materials with fast oxygen reduction reaction kinetics and good stability at high steam pressures, which limits the use of

many conventional air electrodes from SOCs [3]. One material class reported as promising positrode is lanthanide barium cobaltite [3–12]. In order to further improve the surface kinetics of these double perovskites, decoration with oxide nanoparticles created via the exsolution method has been recently reported [3, 10, 13–15].

Functionalization via the exsolution method has been attracting attention in the last decade, especially metal nanoparticle exsolution for SOCs [16–20]. However, oxide-nanoparticle exsolution is a much less explored field [21]. Tsvetkov *et al* [22] reported the formation of nanoparticles of around 30–40 nm diameter from $PrBaCo_2O_{6-\delta}$ after treatment in $pO_2 \sim 10^{-3}$ atm. The authors could not ascribe the nature of the exsolved particles via elemental analyses, but using thermodynamic calculations suggested them to be Co_3O_4 or CoO [22]. Oxide exsolution was triggered by annealing at low pO_2; however, in some cases, these types of double-perovskite cobaltites often present phase segregations in the pristine sample. For instance, Malyshkin *et al* reported the presence of $BaCo_{1-x}Gd_xO_{3-\delta}$ exsolved nanoparticles on as-synthesized La-doped $GdBaCo_2O_{6-\delta}$ [23]. This fact adds complexity to the design of exsolved-functionalized lanthanide-doped barium cobaltites since, in many cases, the perovskite surface is already populated by nanoparticles that are segregated during the synthesis process and that cannot be detected with common laboratory-based x-ray diffractometers. Phase separations during synthesis, occurring in air, can intentionally yield dual-phase composites via exsolution, as seen in the controlled decomposition of $La_{0.3}Ba_{0.7}Zr_{0.4}Co_{0.6}O_{2.75-\delta}$ in air, resulting in a composite formed by $La_{1-x}Ba_xCoO_{3-\delta}$ and $BaZr_{1-y}Co_yO_{3-\delta}$ nanoparticles [11].

Unlike metal nanoparticle exsolution, where the exsolution of multiple elements can be easily controlled to form metallic alloyed nanoparticles [17, 24], the exsolution of multiple elements in the form of oxides can lead to the formation of individual oxide nanoparticles with different compositions. These nanoparticles may have different electrocatalytic properties, so it is important to have processing guidelines to finely control the oxide-nanoparticle exsolution. For instance, the exsolution of $BaCoO_3$ [3, 10, 15], from $PrBa_{0.8}Ca_{0.2}Co_2O_{5+\delta}$ has been confirmed, whereas Tsvetkov *et al* ascribed the particles to binary cobalt oxide exsolution [22]. In a recent work, the exsolution of perovskite nanoparticles from Lu-doped of $Ba_{0.5}La_{0.5}CoO_3$ is reported [25]. Park *et al* found the presence of exsolved $BaCoO_3$ after treatment in wet air at 750 °C, which improved the electrocatalytic activity. More recently, the exsolution of BaO_x from $K_{0.05}Ba_{0.95}Co_{0.4}Fe_{0.4}Zr_{0.18}Y_{0.02}O_{3-\delta}$ boosted the electrocatalytic activity [26]. There are still questions about how the gas atmosphere and temperature affect exsolved nanoparticles. However, it is worth mentioning that Tsvetkov *et al* could not confirm the nature of the exsolved nanoparticles [22]. Conventional metallic exsolution usually is controlled by adjusting external factors (e.g. temperature, time, gas composition) [27], or intrinsic material properties (A-site deficiency [28], B-site composition [29], strain [30]). However, there is still little knowledge on how adjusting these parameters could help control oxide nanoparticle exsolution.

In this work, we expand our understanding of the factors influencing oxide exsolution in $PrBaCo_2O_{6-\delta}$ materials by investigating the impact of A-site deficiency on nanoparticle exsolution. This has primarily two motivations: (i) Ba-deficient $PrBaCo_2O_{6-\delta}$ materials exhibit better electrochemical properties than the stoichiometric composition [31]; and (ii) A-site deficiency is typically practiced to boost exsolution of metallic nanoparticles [16, 28]. For that purpose, a series of Ba-deficient $PrBa_{1-x}Co_2O_{6-\delta}$ with $x = 0$, 0.05, 0.1, 0.15 were synthesized and thoroughly characterized via conventional techniques and synchrotron-based small angle x-ray scattering (SAXS), a tool, which despite its potential, has been scarcely employed in the field of exsolution [32].

2. Experimental methods

2.1. Materials preparation
Double perovskites $PrBa_{1-x}Co_2O_{6-\delta}$ ($x = 0$, 0.05, 0.1, 0.15) were prepared through a modified Pechini sol–gel route via nitrate precursors using $Pr(NO_3)_3 \cdot 6H_2O$, $Ba(NO_3)_2$, and $Co(NO_3)_2 \cdot 6H_2O$ and citric acid from Sigma-Aldrich and following a synthetic protocol previously described [17]. The obtained powders were ground in a mortar in acetone and further treated at 1100 °C for 48 h with a heating rate of 5 °C min^{-1} under static air conditions.

2.2. Physicochemical characterization
X-ray diffractometry (XRD) was carried out with a PANalytical CubiX as described in [33] and Rietveld refined [34] with X'Pert Highscore Plus software (version 3.0.0). Raman spectroscopy was performed with a Renishaw Raman spectrometer (New Mills, UK). Analyses were conducted at room temperature with a 514 nm laser equipped with an Olympus microscope and a CCD detector. Raman active modes for each symmetry group were obtained at the Bilbao Crystallographic Server [35].

Scanning electron microscopy (SEM) characterization was done with a GeminiSEM 500 from Zeiss. Image analyses were performed with Image J software (Version 1.52a) [36].

Scanning transmission electron microscopy (STEM) was performed using a FEI Titan G2 60–300 kV as described in [25], and with a JEM2100F 200 kV as described in [33]. Thermogravimetric analyses were performed in a NETSZCH STA 449 thermobalance, measuring from room temperature to 1000 °C under either synthetic air or N_2 flow.

2.3. *Ex situ* SAXS

Ex situ SAXS and wide-angle x-ray scattering (WAXS) was performed at the SAXSMAT beamline P62, PETRA III, DESY, Hamburg, Germany, at an x-ray energy of 12 keV [37]. The sample-detector-distance from the center of the capillary was calibrated using silver behenate powder mounted in the same setup under ambient conditions. *Ex situ* measurements were performed with the sample powders after corresponding heat treatments in the lab, and the powders were placed in a sample holder under ambient conditions. For the analysis, a background correction was performed, and data were calibrated with Plexiglas for SAXS and silicon for WAXS measurements. As the volume fraction determination from SAXS strongly depends on the scattering contrast, $\Delta\rho$ [38], which depends on the chemical composition of nanoparticles and surrounding material, relative units are used for the vol.% determination, always assuming the same scattering contrast (no changes in the composition of both precipitates and surrounding material regardless the heat treatment).

For the analysis of the SAXS data, the exsolved nanoparticles were fitted with the SASFit software [39], assuming the form factor of ellipsoidal particles with lognormal particle size distribution of both axes. Size data obtained from SAXS and shown in the graphs correspond to the mean size of both axes obtained from the lognormal size distribution. The data evaluation of WAXS data was performed using Rietveld refinement using Fullprof [40].

3. Results

3.1. Influence of Ba deficiency on the crystal structure and oxygen content

The x-ray diffractograms of the four as-synthesized $PrBa_{1-x}Co_2O_{6-\delta}$ ($x = 0$, 0.05, 0.1, 0.15) samples are shown in figure 1(a). Table 1 depicts the crystallographic data of the four samples, extracted via Rietveld refinement (figure S1). All the samples presented a tetragonal double-perovskite structure with *P4/mmm* symmetry, as previously reported [31]. There is no sign of secondary phases appearing by XRD, however, at this point, secondary oxide traces of small size not detectable with the used equipment could not be disregarded. There is a slight peak shift toward higher 2θ values upon an increase in the A-site deficiency (figure 1(a)), consistent with previous works on Ba-deficient $PrBaCo_2O_{6-\delta}$ [41]. This is ascribed to a lattice shrinkage, further confirmed by the cell volume values shown in table 1, i.e. the lattice volume decreases from 116.13 Å³ ($PrBaCo_2O_{6-\delta}$) to 115.64 Å³ ($PrBa_{0.85}Co_2O_{6-\delta}$). As a general trend, Ba deficiency causes a shortening of the *a* and/or *c*-axis of the tetragonal double-perovskite cell, although no clear trend could be inferred.

Figure 1(b) depicts the weight loss curves for the four $PrBa_{1-x}Co_2O_{6-\delta}$ samples upon heating to 1000 °C in air. Here, the influence of Ba deficiency on the oxygen exchange capacity was assessed via thermogravimetry under oxidizing conditions (air flow). First, a weight gain can be observed up to the 275 °C–300 °C range, which can be ascribed to a slight sample re-oxidation (refilling of oxygen vacancies formed during sintering at 1100 °C). It should be noted that for PBC, there was an initial apparent weight loss at low temperatures, probably due to an experimental artifact or a higher amount of water adsorbed released at this temperature range. Interestingly, the temperature at which this initial weight gain reached a maximum followed a trend with Ba deficiency: PBC85 reached it at 277 °C, whereas for PBC95 it was 312.5 °C. From this point on, there is a gradual weight loss related to the release of lattice oxygen, the reduction of Co^{4+} cations, and the formation of oxygen vacancies. The total weight loss for these materials was 1.16%, 1.34%, 1.35%, and 1.33% for PBC, PBC95, PBC90, and PBC85, respectively. However, the A-site deficient materials exhibit a second weight loss event occurring around 900 °C. These second weight losses (which are lumped in the previous values) were 0.24%, 0.265%, and 0.34% for PBC95, PBC90, and PBC85, respectively, indicating that this second event was more pronounced when increasing the A-site deficiency. This second weight loss event was much faster than the gradual lattice oxygen release, and even if observed in previous works [31], its nature is unknown. A possible reason could be the reduction of Co_3O_4, traces that could not be inferred by XRD, to form CoO, which usually occurs in this temperature range [42]. This could be linked to the fact that increasing the Ba deficiency makes the system more likely to form cobalt oxide phase segregations. Since tetragonal weight loss is associated with this process, it is unlikely that this will be related to just a crystallographic phase transition, e.g. from tetrahedral to orthorhombic phases, as described later. Thus, by subtracting the weight loss assigned to this second event, which might not imply the generation of oxygen vacancies, the actual weight loss values ascribed to the release of lattice oxygen from the double perovskite were 1.16%, 1.098%, 1.083%, and 0.984%, for PBC, PBC95, PBC90, and PBC85, respectively.
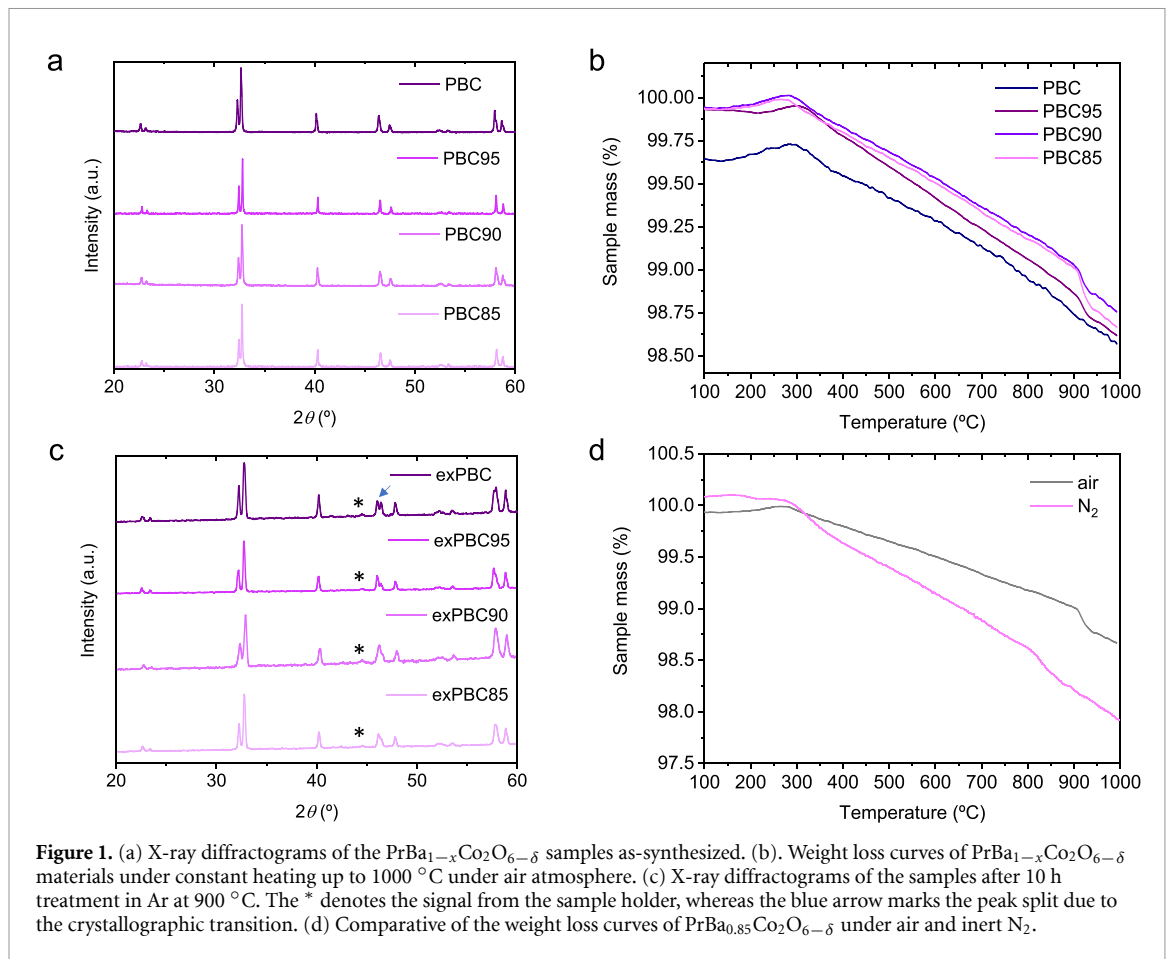
Figure 1. (a) X-ray diffractograms of the $PrBa_{1-x}Co_2O_{6-\delta}$ samples as-synthesized. (b). Weight loss curves of $PrBa_{1-x}Co_2O_{6-\delta}$ materials under constant heating up to 1000 °C under air atmosphere. (c) X-ray diffractograms of the samples after 10 h treatment in Ar at 900 °C. The * denotes the signal from the sample holder, whereas the blue arrow marks the peak split due to the crystallographic transition. (d) Comparative of the weight loss curves of $PrBa_{0.85}Co_2O_{6-\delta}$ under air and inert N_2.

Table 1. Crystallographic data of the as-synthesized $PrBa_{1-x}Co_2O_{6-\delta}$ samples.

Label	Formula	Cell volume ($Å^3$)	$a = b$ (Å)	c (Å)	Space group
PBC	$PrBaCo_2O_{6-\delta}$	116.13	3.9006 ± 0.0002	7.6327 ± 0.0004	P4/mmm
PBC95	$PrBa_{0.95}Co_2O_{6-\delta}$	116.14	3.9009 ± 0.0002	7.6325 ± 0.0004	P4/mmm
PBC90	$PrBa_{0.90}Co_2O_{6-\delta}$	115.85	3.8963 ± 0.0003	7.6315 ± 0.0007	P4/mmm
PBC85	$PrBa_{0.85}Co_2O_{6-\delta}$	115.64	3.8918 ± 0.0002	7.6366 ± 0.0004	P4/mmm

These results indicate that, under oxidizing conditions, the oxygen content in the $PrBa_{1-x}Co_2O_{6-\delta}$ materials decreases with increasing the Ba deficiency, which matches well with previous reports [31].

In order to check the elemental distribution homogeneity of the as-synthesized samples, STEM-EDX analyses were performed. This is exemplified by the PBC and PBC85 sample in figures 2(a) and (b), respectively, which show the high-angle annular dark-field (HAADF)-energy dispersive x-ray analysis (EDX) analysis for these samples. This elemental analysis illustrates the elemental homogeneity of the as-synthesized samples, regardless of the amount of Ba in the A-site.

3.2. Understanding nanoparticle exsolution on $PrBa_{1-x}Co_2O_{6-\delta}$ materials
Exsolution of cobalt metallic nanoparticles from perovskites has been carried out in highly reductive atmospheres, e.g. in H_2 [43]. In order to promote cobalt oxide nanoparticle exsolution, much less reductive conditions should be considered. Indeed, the first reports on cobalt oxide exsolution from PBC were performed at 1000 °C and $pO_2 \sim 10^{-3}$ atm [22]. Here, the as-synthesized samples were initially treated at 900 °C for 10 h in a constant flow of Ar ($pO_2 \sim 10^{-5}$ atm) in order to drive the exsolution of oxide nanoparticles and prevent further reduction to metallic state. In figure 1(c), the XRD patterns of the four samples after treatment in Ar are depicted, evidencing differences when compared to the as-synthesized samples. Specifically, a peak doublet was detected at around $2\theta = 46.5°$, indicating a phase transition from a tetragonal double-perovskite structure to an orthorhombic cell (*Pmmm* space group) [12]. The presence of this peak doublet was more evident for PBC, and it decreases with increasing the Ba deficiency, suggesting that the absence of Ba might slow down this crystallographic transformation. No evidence of secondary
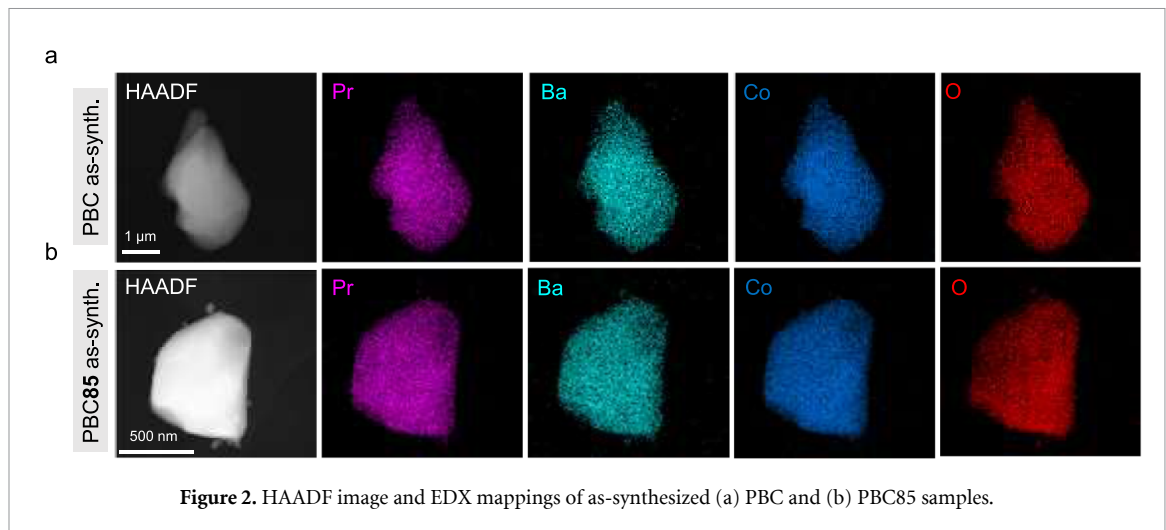
Figure 2. HAADF image and EDX mappings of as-synthesized (a) PBC and (b) PBC85 samples.

phases could be inferred by XRD after the reduction treatment, although, as will be shown later, these materials were populated with nanoparticles of different shapes and compositions. To understand the oxygen loss under inert conditions, the materials were analyzed under a heating ramp to 1000 °C but under inert N_2 conditions. Figure 1(d) illustrates the differences in oxygen exchange between air and inert conditions, exemplified by the PBC85 sample. Lowering the pO_2 increases the total weight loss by 2.14%, whereas under air, the loss was 1.33% considering all the weight loss events. Carrying out the thermal reduction under inert conditions facilitates oxygen vacancy formation, which might promote the exsolution mechanism [44]. The reduction in N_2 also affected the second weight loss event identified at ∼900 °C in air by shifting it to lower temperatures, i.e. the onset temperature was at 800 °C. In addition, the weight loss associated with this process was lower than in air conditions and more gradual. Finally, under inert conditions, there is no weight gain during the initial heating up to 300 °C, which in air was ascribed to an oxidation process.

After identifying the crystallographic changes occurring upon the 10 h treatment at 900 °C in Ar, the morphology changes were assessed via SEM. Figure 3 depicts the images of the four $PrBa_{1-x}Co_2O_{6-\delta}$ samples after the exsolution treatment. It should be noted here that exsolution was performed on the porous as-synthesized powders. The exsolution data gathered from this analysis, such as nanoparticle size, could be extrapolated to porous sintered electrodes in an electrolysis cell, as previously reported [17]. All the samples presented a surface covered by nanoparticles, regardless of the A-site deficiency of the material. However, some differences were observed between the samples. First, for PBC and PBC90, two different types of particles cover the surface. For PBC, some elongated particles of about 50 nm length are present together with the exsolved nanoparticles of about 8 nm size. Note that for distribution purposes, the image analyses were focused on the exsolved nanoparticles with sizes lower than 50 nm. These nanoparticles are more homogeneously dispersed than the larger ones and would present higher catalytic activity due to size effects. The particle size distribution of each sample (figure 3 and histograms in figure 2) reveals that the exsolved nanoparticles tend to populate different parts of the perovskite grains, including edges, terraces, and grain boundaries. However, the analysis of several spots and grains suggests that not all of them are populated by exsolved nanoparticles, and the dispersion is not homogeneous. This is reflected, for instance, in the PBC90 image in figure 2, in which some grains exhibit a large presence of exsolved nanoparticles, whereas in other neighboring grains, there is a total absence of exsolution. Uneven growth of exsolved nanoparticles has also been shown in metallic exsolution in bulk perovskites [45] and, especially, in thin-films [46, 47]. In particular, the work of Kim *et al* showed that plane orientation could greatly affect the shape and dispersion of Ni nanoparticles grown on epitaxial perovskite thin-films [30].

The image of PBC90 also reflects that the nanoparticle size is larger and the distribution broader compared to the other samples (figures 3(c)–(e)). Namely, the mean exsolved particle size for PBC90 was 18 ± 5 nm, whereas for PBC, PBC95, and PBC85, it was 8 ± 3, 8 ± 3, and 8 ± 2 nm, respectively. Data on exsolved nanoparticle dispersion is collected in figure 3(f). The samples presented high heterogeneity from grain to grain in some samples, with highly populated zones and other areas in which nanoparticles were not observed, such as for PBC90. Nevertheless, visual image analyses indicate that A-site deficiency does not necessarily increase the amount of exsolved nanoparticles per unit area. For instance, PBC95 and PBC90 experienced a remarkable decrease in nanoparticle (NP) population if compared to PBC, with 283, 166, and 1195 NPs μm^{-2}, respectively. Interestingly, later, for PBC85, the amount of exsolved nanoparticles further increased with respect to PBC95 and PBC90 but was still lower than for PBC. This is one of the first
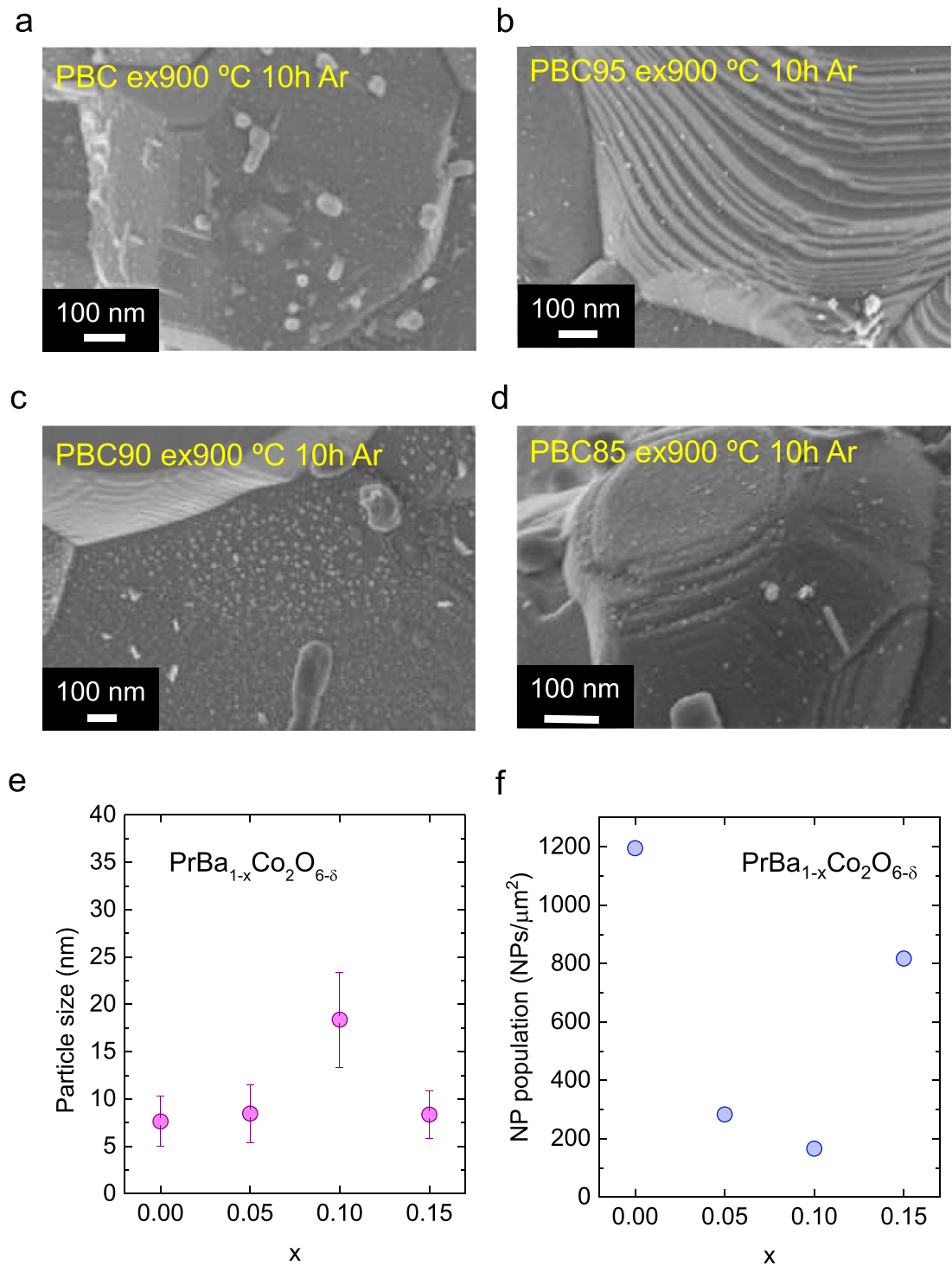
Figure 3. SEM images of (a) $PrBaCo_2O_{6-\delta}$, (b) $PrBa_{0.95}Co_2O_{6-\delta}$, (c) $PrBa_{0.9}Co_2O_{6-\delta}$, and (d) $PrBa_{0.85}Co_2O_{6-\delta}$ after treatment in Ar at 900 °C for 10 h. (e) Average particle size values for all the samples. (f) Nanoparticle dispersion for the different A-site deficient materials synthesized.

differences observed compared to metallic exsolution, in which, conventionally, A-site deficiency has been reported to increase the amount of exsolved nanoparticles, especially for Ni-doped titanates [28, 33]. However, it should be also noted that for some perovskite systems, A-site deficiency has led to a decrease in the number of metallic nanoparticles exsolved. For instance, in $Sr_{2-x}FeCo_{0.2}Ni_{0.2}Mo_{0.5}O_{6-\delta}$, it led to lower dispersions after exsolution. This was ascribed to the formation of NiO segregations in the pristine samples with decreasing the Sr content, thus, limiting the amount of exsolvable Ni in the host lattice [17]. Also, in thin films, Weber reported a decrease in the Ni exsolution extent ascribed to crystallographic distortions caused by the A-site non-stoichiometry [48]. Furthermore, the exsolved oxide nanoparticles do not present
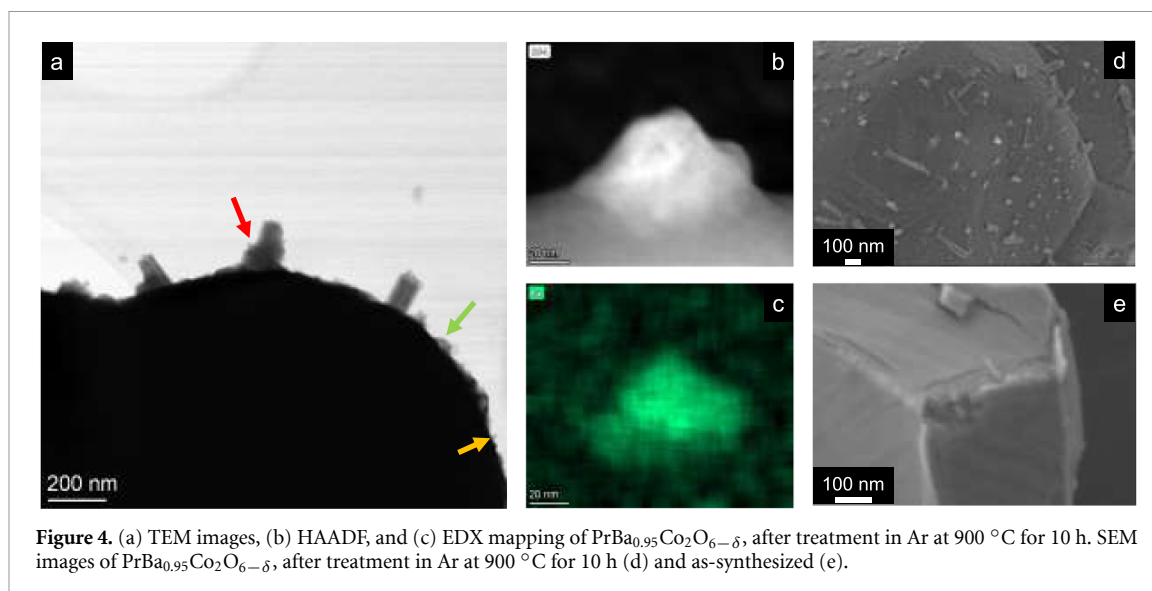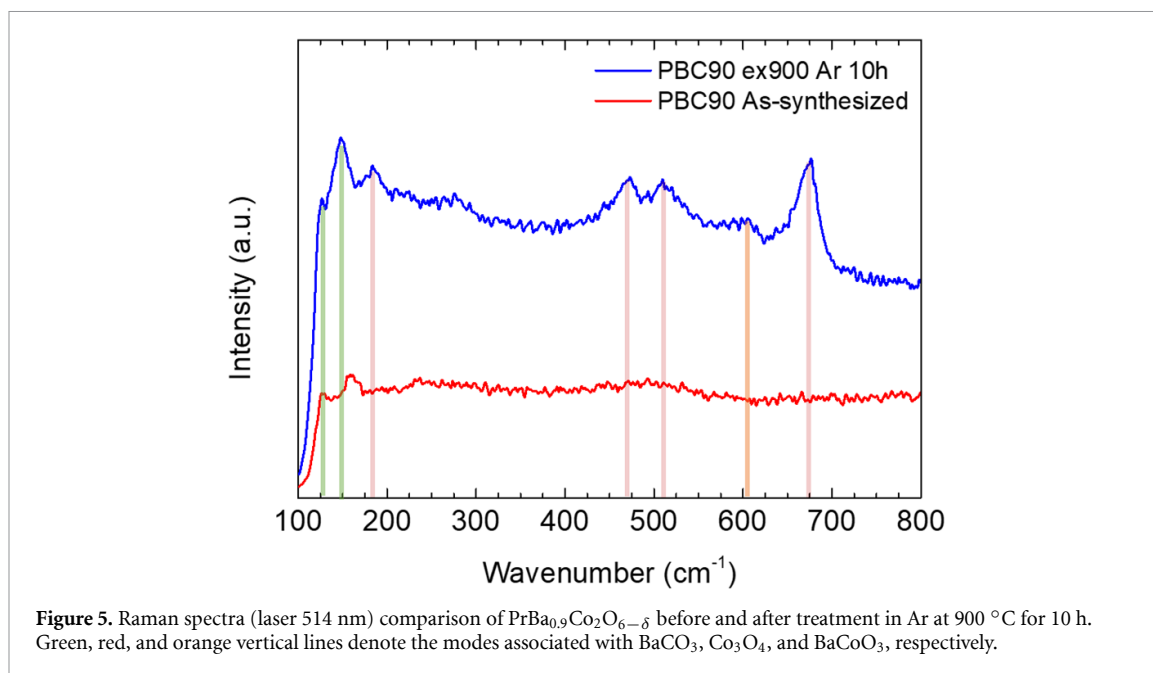
Figure 4. (a) TEM images, (b) HAADF, and (c) EDX mapping of $PrBa_{0.95}Co_2O_{6-\delta}$, after treatment in Ar at 900 °C for 10 h. SEM images of $PrBa_{0.95}Co_2O_{6-\delta}$, after treatment in Ar at 900 °C for 10 h (d) and as-synthesized (e).

the classic spherical shape observed for metallic particles exsolved in H_2, albeit metallic nanoparticles can adopt different shapes depending on the actual exsolution conditions [49, 50].

In this work, the particles that populate the surface of the $PrBa_{1-x}Co_2O_{6-\delta}$ perovskite materials exhibit different sizes and shapes, suggesting the presence of various compositions. Transmission electron microscopy (TEM) analysis (figure 4(a)) of the PBC95 treated in Ar reveals at least three different particle morphologies populating the perovskite surface. The first type of nanoparticles is exemplified by the one marked with the yellow arrow in figure 4(a). These particles are around 8 nm in size and are the exsolved particles mentioned in the previous section (Type I). The second class is the one pointed with a green arrow. These particles are amorphous (figure 4(b)), and EDX analysis confirmed that they were mainly formed by Ba (figure 4(c)). These are probably amorphous BaO oxide precipitates that tend to react with atmospheric CO_2, forming $BaCO_3$, and could be a side-effect of the exsolution process, as recently shown in the literature [51]. These pointy particles of around 50 nm size were also observed in SEM analyses (figure 4(d)), especially in grains in which the exsolved nanoparticles of around 8 nm were present. Figure 4(e) shows the morphology of the as-synthesized PBC95 grain without any nanoparticles present on the surface. Finally, nanoprism-like particles are about 125–160 nm long and 60–100 nm wide. EDX point analysis of the composition of the nanoparticle marked with the red arrow (table S1 in the supporting information) shows that these particles are mainly composed of Ba, Co, and O, with a minor contribution of Pr, suggesting that these elongated particles might be $BaCoO_3$ segregations, as previously reported for similar double perovskites [1].

Raman spectroscopy was employed to further structurally characterize the oxide-nanoparticle exsolution mechanism in $PrBa_{1-x}Co_2O_{6-\delta}$ perovskites. Unlike the case of metal nanoparticle exsolution, Raman spectroscopy can be very useful in determining the species evolving in oxide exsolution [3, 14, 15]. The spectra of the four $PrBa_{1-x}Co_2O_{6-\delta}$ series can be found in figures S3 and S4, respectively. All the as-synthesized samples (figure S2) present identical Raman spectra, and only a sharp peak can be identified at around 155 cm^{-1} for the four samples. In addition, the samples presented two humps in the 300–350 cm^{-1} and 500–550 cm^{-1} regions. Previous reports did not report any Raman signal for similar compositions because materials that crystallize in *P4/mmm* symmetry show little Raman activity [10]. Specifically, materials in the symmetry group *P4/mmm* has six Raman active modes ($2A_{1g} + B_{1g} + 3E_g$), whereas *Pmmm* symmetry exhibits 24 active modes ($8A_g + 3B_{1g} + 5B_{2g} + 8B_{3g}$) [35]. Thus, the low Raman activity of pristine $PrBa_{1-x}Co_2O_{6-\delta}$ materials points to an additional phase appearing in the Raman spectra. This mode around 150 cm^{-1} might be associated with a $BaCO_3$ phase appearing due to exposure of $PrBa_{1-x}Co_2O_{6-\delta}$ materials to ambient conditions. Indeed, Kaabar *et al* reported two Raman features of $BaCO_3$ appearing at 135 and 153.2 cm^{-1} [52]. It was difficult to ascribe other Raman modes to the humps at 300–350 cm^{-1} and 500–550 cm^{-1} due to the broad shape of these minor contributions.

After exsolution in Ar, new Raman modes (figure S3) become visible for all the samples, and differences can be inferred between them. PBC90 and PBC85 present almost identical spectra. In order to exemplify the difference between the as-synthesized and exsolved samples, figure 5 shows a comparison for PBC90. The mode ascribed to $BaCO_3$ is still present, slightly shifting to lower wavenumbers (152 cm^{-1}). Then, several modes that could be ascribed to Co_3O_4 were found at 675 (A_{1g}), 614 (F_{2g}), 470 (F_{2g}), 513 (E_g), and 183 cm^{-1}

Figure 5. Raman spectra (laser 514 nm) comparison of $PrBa_{0.9}Co_2O_{6-\delta}$ before and after treatment in Ar at 900 °C for 10 h. Green, red, and orange vertical lines denote the modes associated with $BaCO_3$, Co_3O_4, and $BaCoO_3$, respectively.

(F_{2g}) [53, 54]. These modes are slightly shifted to lower wavenumbers compared to literature data [53, 54]. However, it has been previously reported that Raman modes of Co_3O_4 nanoparticles presented a redshift (and broader peaks) if compared to micron-size particles [55]. Finally, a mode at ca. 607 cm^{-1} is ascribed to $BaCoO_3$ perovskite [56]. According to the Raman mode assignment, the presence of $BaCO_3$, Co_3O_4, and $BaCoO_3$ on the perovskite surface can be confirmed after the Ar treatment. This aligns with the TEM observations, indicating at least three different types of particles, as shown in figure 4(a).

The Raman spectra for PBC and PBC95 show slight differences compared to PBC90 and PBC85, as illustrated in figure S3. First, for PBC90 the mode at ca. 675 cm^{-1}, which is the most prominent Co_3O_4 feature, decreases abruptly in intensity and for PBC disappears. This suggests that the presence of Co_3O_4 increases with increasing the Ba deficiency. This hypothesis aligns with the thermogravimetric analysis (TGA) results in figure 1(b), where the A-site deficient materials exhibited a decomposition above 900 °C initially attributed to the reduction of Co_3O_4 to form CoO. This weight loss was higher for PBC85 and PBC90 compared to PBC95, indicating that these two samples would have a higher presence of Co_3O_4. Figure S3 also indicates that the peak intensity at around 150 cm^{-1} increased with the Ba content, demonstrating the positive effect of Ba deficiency in preventing the formation of barium carbonates. PBC95 displayed a broad mode from 400 to 600 cm^{-1}, lumping several modes, making their assignment challenging. However, it is important to note that both PBC and PBC95 exhibited a higher extent of transformation from the *P4/mmm* to the *Pmmm* symmetry (figure 1(c)), which is more Raman active. Therefore, several of these features will correspond to *Pmmm* symmetry, although no references in literature were found to accurately ascribe each Raman mode.

3.3. Effect temperature on the nanoparticle exsolution

In the previous sections, the focus was put on assessing the influence of Ba deficiency on the structural properties and nanoparticle exsolution of $PrBa_{1-x}Co_2O_{6-\delta}$ perovskite materials. It was observed that PBC90 exhibited the largest exsolved particle size with a broad particle size distribution when treated at 900 °C, figure 3.

In metallic nanoparticle exsolution, exsolved nanoparticle size can be diminished by performing the exsolution treatment at lower temperatures [17, 27]. Thus, following a similar strategy, the impact of temperature on the exsolved nanoparticle size was assessed by performing the treatment at 600 °C, 700 °C, and 800 °C. The SEM images in figures 6(a)–(d) display the exsolved nanoparticles on the surface of the PBC90 perovskite grains at four different temperatures. At all temperatures, nanoparticles are observed on the surface of the grains, with a more uniform coverage at lower temperatures (600 °C and 700 °C) compared to higher temperatures (800 °C and 900 °C), where some grain facets do not show exsolution. The particle size distribution for each temperature treatment is shown in figure S5, indicating that decreasing the temperature results in a narrower nanoparticle size distribution. Additionally, the mean particle size decreases as the exsolution temperature is lowered, from 18.4 nm at 900 °C to 9.3 nm at 600 °C. This trend is similar to what is observed in metallic exsolution.
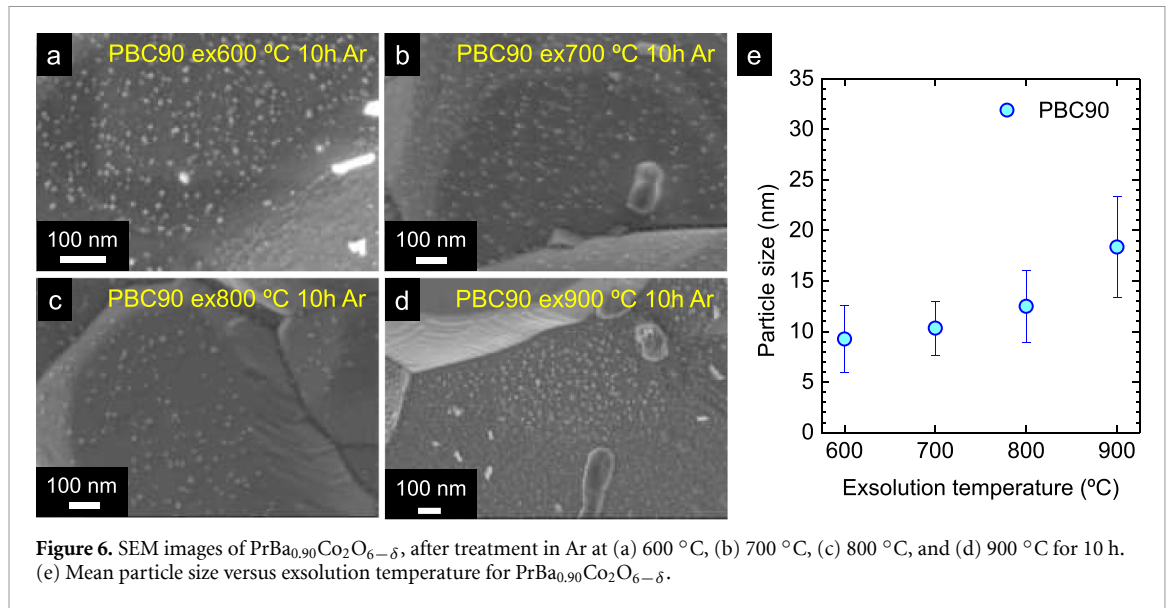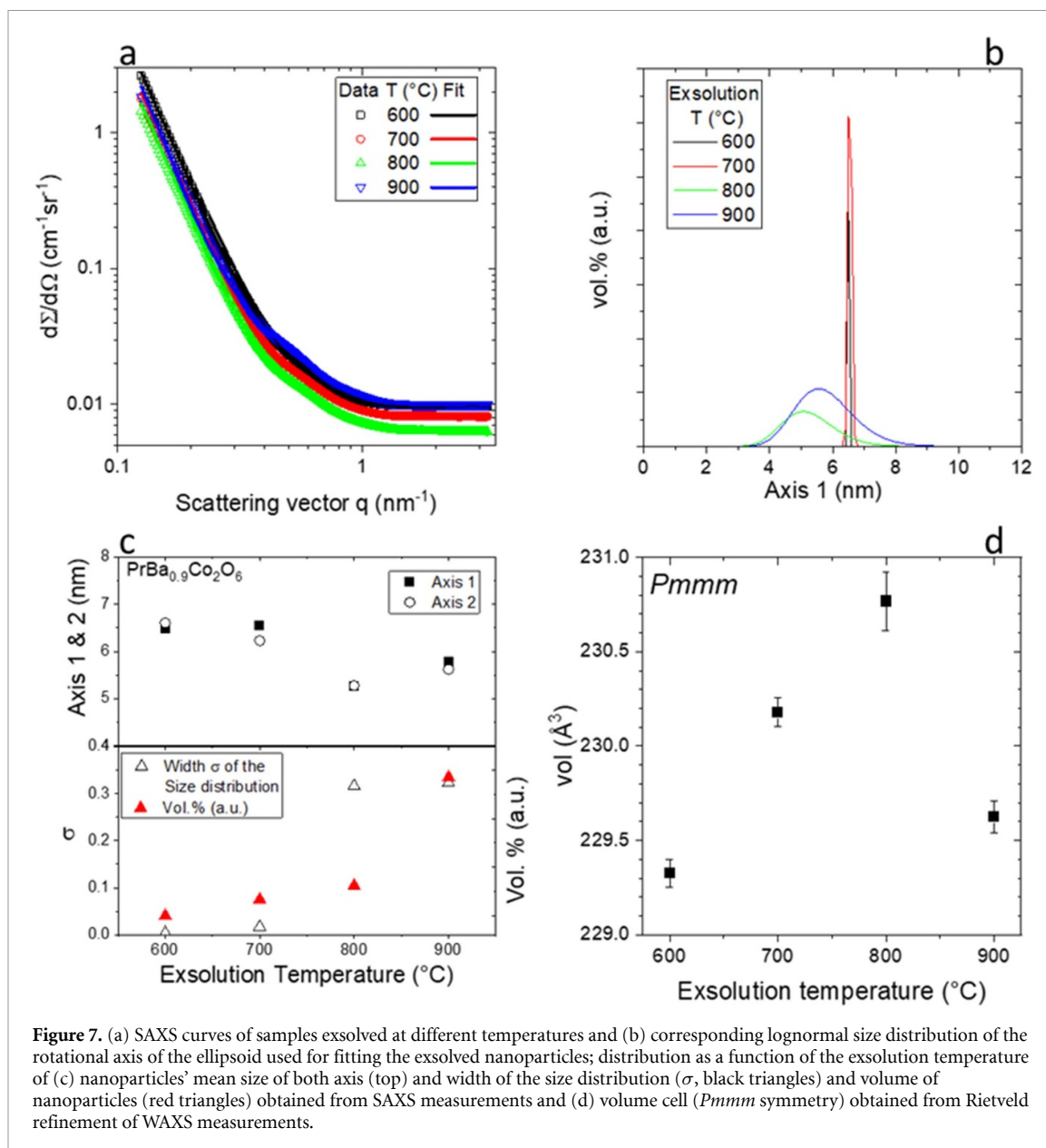
Figure 6. SEM images of $PrBa_{0.90}Co_2O_{6-\delta}$, after treatment in Ar at (a) 600 °C, (b) 700 °C, (c) 800 °C, and (d) 900 °C for 10 h. (e) Mean particle size versus exsolution temperature for $PrBa_{0.90}Co_2O_{6-\delta}$.

Synchrotron SAXS-WAXS experiments were conducted to investigate the nanoparticle exsolution in PBC90 *ex-situ*, using the PBC90 sample treated at different temperatures. SAXS measurements (figure 7(a)) were fitted assuming ellipsoidal nanoparticles constituted by a major and a minor axis. The obtained lognormal size distributions for one of the axes are shown in figure 7(b). Results indicate that the ellipsoidal nanoparticles present mean sizes of both axes (figure 7(c) top) with less than 10% difference. Obtained mean sizes of around 6 nm decrease with the exsolution temperature [32, 57] although the particle size distribution becomes broader with the temperature, as it goes from 1 nm at 500 °C–700 °C to 4 nm at 800 °C–900 °C. This broader distribution is shown in figure 7(b) (and the width parameter of the distribution in figure 7(c) bottom) and is like the trend observed in the SEM images in figure 6, although the SEM data reflects slightly smaller particles as it provides area-weighted dimensions, while the SAXS provides volume-weighted sizes. Besides, assuming the same scattering contrast between exsolved nanoparticles and bulk material, the volume fraction of the exsolved particles increases slightly except at 900 °C, where a significant increase is observed (figure 7(c) bottom right). The broader size distribution and vol.% at 900 °C could be easily linked to the faster exsolution kinetics at this temperature, resulting in a higher amount of small exsolved nanoparticles [30] and also to the coarsening of more of them when comparing the same times at lower temperatures. The RT WAXS patterns of the PBC90 *ex-situ* exsolved at different temperatures (figure S6) display a double-perovskite structure with *Pmmm* symmetry, consistent with the observed Raman results. The lattice parameters obtained from Rietveld refinement of the different RT patterns show a continuous increase in the lattice cell volume with increasing exsolution temperature except for the sample exsolved at 900 °C, which shows a shrinkage of the lattice volume.

4. Discussion

In this work, we have evaluated the oxide nanoparticle exsolution via reductive treatments in Ar atmospheres at mild pO_2 conditions. This differs from metallic nanoparticle exsolution in which lower pO_2 is required for a full reduction of the metal transition cations to their metallic counterparts. Here it should be noted that one of the first works on oxide exsolved nanoparticles utilized a different approach than here. The work by Neagu *et al* [58] used metallic exsolution to create well-anchored CoNi alloys and observed that, under $CO + O_2$ atmosphere used for CO combustion reactions, these particles evolved to $(Co,Ni)_3O_4$ spinels. This also came with a morphological variation from spherical to more polyhedral hollow structures, which, upon an increase in CO concentration, evolved into prismatic shapes. With this elegant approach, oxide NPs of 10 or 30 nm were obtained, with dispersions of around 700 and 150 NP μm^{-2}, respectively. In the present work, the size of Type I nanoparticles was between 5 and 20 nm, whereas dispersion ranges were broad depending on the A-site deficiency, varying between 166 to 1195 NP μm^{-2} for PBC90 and PBC, respectively. Importantly, the work of Neagu *et al* produced solely spinels as exsolved particles, whereas in direct oxide exsolution works, such as the present, a wide variety of compositions such as BaO_x [26], CoO_x [22], and $BaCoO_3$ [3] or other related perovskites have been identified.

Continuing with the differences with metallic exsolution, we should consider the working pO_2. In metallic exsolution, the formation of nanoparticles is performed, normally, under very reducing

Figure 7. (a) SAXS curves of samples exsolved at different temperatures and (b) corresponding lognormal size distribution of the rotational axis of the ellipsoid used for fitting the exsolved nanoparticles; distribution as a function of the exsolution temperature of (c) nanoparticles' mean size of both axis (top) and width of the size distribution (σ, black triangles) and volume of nanoparticles (red triangles) obtained from SAXS measurements and (d) volume cell (*Pmmm* symmetry) obtained from Rietveld refinement of WAXS measurements.

atmospheres by using (diluted) hydrogen, with $pO_2 \sim 10^{-20}$ atm. For oxide exsolution, the working pO_2's are several orders of magnitudes higher. Values range from $\sim 10^{-5}$ atm used in this work to $10^{\sim 3}$ atm used in the pioneering work of Tsvetkov *et al* [22] or more recently in wet air conditions $pO_2 = 0.21$ atm in the work of Park *et al* in which BaO_x [26] NPs were exsolved. Indeed, we should consider the wide variety of different structures reported in oxide exsolution literature. This implies that the mechanism of each type of exsolved chemistry, that is, alkaline-earth oxide (BaO_x), spinel (Co_3O_4), or perovskite ($BaCoO_3$), might be governed by different physicochemical mechanisms, composition, temperature, and pO_2 dependencies. Furthermore, BaO_x phases can be also considered precursors of $BaCO_3$ carbonate phases. Some reports also considered the direct formation of barium carbonates in proton conductors when exposed to industrial Ar at 800 °C [59]. Alternatively, barium carbonates can already appear due to contact with ambient air when stored, as precluded by the Raman analyses of the pristine samples, see figure 5.

Returning to the pO_2 dependence, the mild pO_2 used in this work will thermodynamically not lead to the formation of metallic cobalt. However the reduction of cobalt cations can lead to the formation of other species with intermediate oxidation states.

PBC can be taken to be a double perovskite with Co average oxidation state $+3.5$. The oxygen stoichiometry is generally $6 - \delta > 5.5$ so that it is dominated by Co^{4+} states with effective charge $+1/2$ and Kröger–Vink notation $Co_{Co}^{\frac{1}{2}\bullet}$ over Co^{3+} states with effective charge $-1/2$ and notation $Co_{Co}^{\frac{1}{2}'}$, and then the reduction to form more oxygen vacancies may be written [60]
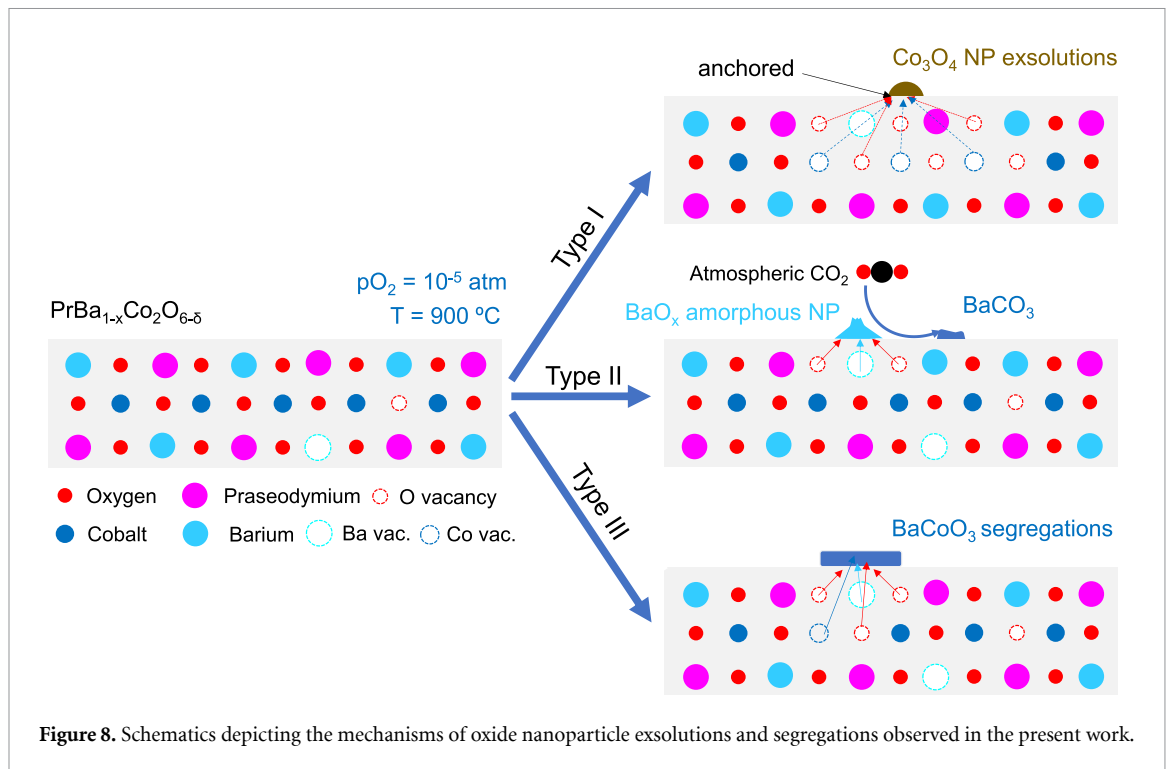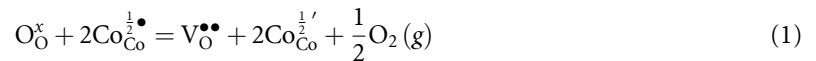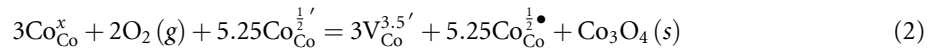
Figure 8. Schematics depicting the mechanisms of oxide nanoparticle exsolutions and segregations observed in the present work.

$$O_O^x + 2Co_{Co}^{\frac{1}{2}\bullet} = V_O^{\bullet\bullet} + 2Co_{Co}^{\frac{1}{2}\prime} + \frac{1}{2}O_2\,(g) \tag{1}$$

where O_O^x and $V_O^{\bullet\bullet}$ denote lattice oxygen and oxygen vacancy, respectively (here not distinguishing different oxygen sites in the double perovskite). The oxygen vacancies formed may serve as surface nucleation sites to enable the exsolution as suggested in the work of Wang *et al* [44].

The exsolution of spinel cobalt oxide (Co_3O_4) will then proceed, leaving behind cobalt vacancies with an average effective charge of -3.5. Charge balance may be preserved through oxidation, like

$$3Co_{Co}^x + 2O_2\,(g) + 5.25Co_{Co}^{\frac{1}{2}\prime} = 3V_{Co}^{3.5\prime} + 5.25Co_{Co}^{\frac{1}{2}\bullet} + Co_3O_4\,(s) \tag{2}$$

or through the formation of oxygen vacancies, which by the combination of equations (1) and (2) can be seen to represent reduction,

$$3Co_{Co}^x + 5.25O_O^x = 3V_{Co}^{3.5\prime} + 5.25V_O^{\bullet\bullet} + Co_3O_4\,(s) + 0.625O_2\,(g) \tag{3}$$
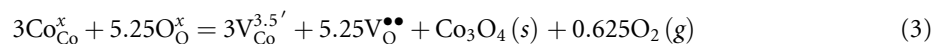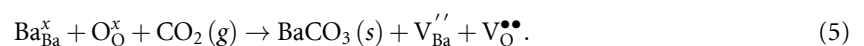
and is illustrated in figure 8.

Concomitantly, instabilities in the lattice can also lead to the formation of other species in which a reduction process is not necessarily driving the nanoparticle formation, such as the formation of BaO (figure 8):
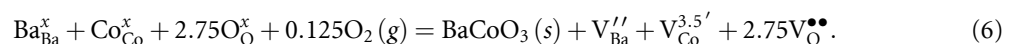
$$Ba_{Ba}^x + O_O^x \rightarrow BaO\,(s) + V_{Ba}^{\prime\prime} + V_O^{\bullet\bullet}. \tag{4}$$

In the presence of $CO_2(g)$, excess Ba will exsolve as barium carbonate:

$$Ba_{Ba}^x + O_O^x + CO_2\,(g) \rightarrow BaCO_3\,(s) + V_{Ba}^{\prime\prime} + V_O^{\bullet\bullet}. \tag{5}$$

This could proceed as a subsequent step of carbonatization of the exsolved BaO, e.g. during storage and other exposure to ambient conditions in which amorphous exsolved BaO species react with CO_2 forming $BaCO_3$ (figure 8).

Finally, the third type of exsolved oxide reported in literature is $BaCoO_3$ (figure 8). The formation of these exsolutions can be written:

$$Ba_{Ba}^x + Co_{Co}^x + 2.75O_O^x + 0.125O_2\,(g) = BaCoO_3\,(s) + V_{Ba}^{\prime\prime} + V_{Co}^{3.5\prime} + 2.75V_O^{\bullet\bullet}. \tag{6}$$

However, in our work, the identified $BaCoO_3$ structures are attributed to a segregation rather than an exsolution. These elongated nanoparticles seem to be completely located outside the perovskite host matrix

rather than anchored into its surface, see figure 3(a), for instance. In a recent work by Wang *et al* [61] the authors reported the concomitant formation of BaO_x and Cu exsolutions, preceded by an initial formation of barium cuprates. This exsolution was performed by reducing $Ba_{0.95}Ce_{0.5}Zr_{0.3}Y_{0.14}Cu_{0.06}O_{3-\delta}$ under 5% H_2 atmosphere and the authors also observed the formation of three different types of phases, confirming the complexity of exsolution in barium-containing perovskites. However, based on the experimental observations of the present work, it is rather unlikely that BaO and Co_3O_4 exsolutions come from the decomposition of $BaCoO_3$, since, and unlike the work of Wang *et al* [61] these two phases are located in separated spots rather than in their vicinity.

In the frame of the present work, the observed trends lead to the conclusion that higher A-site deficiency leads to a decrease of Type I nanoparticle exsolution, probably favoring other segregations. However, this trend was not linear (figure 3(f)) since, for PBC85, the dispersions were more similar to the obtained values for PBC. This further increase in A-site deficiency may facilitate the exsolution mechanism of equation (2) by balancing the amount of B-site vacancies. On the other hand, for PBC this will be done by an increased number of BaO exsolutions that will compensate the cobalt cationic vacancies. To discern the actual mechanism governing oxide exsolution *in situ* techniques, such as *in situ* TEM, XRD, or near ambient pressure x-ray photoelectron spectroscopy (NAP-XPS), would be required to couple the morphological evolution of the nanoparticles during exsolution (nucleation and growth) with the nature of the exsolved species (e.g. oxidation species, coordination). This information will be extremely helpful for identifying the onset point for the formation of each and eventually quantifying the concentration of each one. In addition, these techniques, coupled with computational tools (e.g. density functional theory (DFT)), could be helpful for identifying the amount of each nanoparticle species on the perovskite surface, which will add valuable information about the most energetically favored and prevalent mechanism(s).

5. Conclusions

Oxide exsolution from $PrBa_{1-x}Co_2O_{6-\delta}$ double perovskites has been evaluated, paying particular attention to the effects of A-site deficiency and variations in the temperature treatment on the nanoparticle properties. Unlike in metallic exsolution, A-site deficiency did not help increase the number of exsolved nanoparticles. A slight increase in particle size was observed with increasing the reducing temperature under inert conditions ($pO_2 \sim 10^{-5}$ atm). Interestingly, nanoparticles of different shapes and compositions were observed via TEM and SEM. At least three different nanoparticle types were detected on the surface of $PrBa_{1-x}Co_2O_{6-\delta}$ double perovskites, namely $BaCoO_3$, $Co_3O_{4,}$ and $BaCO_3$, whose nature was further corroborated by Raman spectroscopy. These results reveal that oxide-nanoparticle exsolution is a much more complex phenomenon than metallic exsolution, in which oxide reduction thermodynamics in H_2 is a proper initial predictor for designing exsolved metallic nanocatalysts. On the other hand, oxide-nanoparticle exsolution in double perovskites can occur at much higher pO_2 levels and may result in the exsolution of perovskites, spinels, or amorphous carbonate phases. Several of these phases may contain multiple cations present in the pristine double perovskite. More mechanistic studies—coupling experimental characterization and theoretical modeling—are required to define oxide exsolution guidelines that could result in functionalized electrodes with higher electrocatalytic activity.

Data availability statement

All data that support the findings of this study are included within the article (and any supplementary files).

ORCID iDs

Alfonso J Carrillo ● https://orcid.org/0000-0002-5576-9277
María Balaguer ● https://orcid.org/0000-0002-7098-9235
Cecilia Solís ● https://orcid.org/0000-0002-3997-8802
Andrés López-García ● https://orcid.org/0000-0001-9719-606X
Blanca Delgado-Galicia ● https://orcid.org/0009-0004-4655-5789
Einar Vøllestad ● https://orcid.org/0000-0002-9895-1060
Sebastian Wachowski ● https://orcid.org/0000-0003-3752-0432
Truls Norby ● https://orcid.org/0000-0003-0909-0439
Jose M Serra ● https://orcid.org/0000-0002-1515-1106

References

[1] Vøllestad E, Strandbakke R, Tarach M, Catalán-Martínez D, Fontaine M-L, Beeaff D, Clark D R, Serra J M and Norby T 2019 *Nat. Mater.* **18** 23–26
[2] Duan C, Huang J, Sullivan N and O'Hayre R 2020 *Appl. Phys. Rev.* **7** 011314
[3] Zhou Y *et al* 2021 *ACS Energy Lett.* **6** 1511–20
[4] Tarancón A, Marrerolopez D, Penamartinez J, Ruizmorales J and Nunez P 2008 *Solid State Ion.* **179** 611–8
[5] Kim G, Wang S, Jacobson A J, Reimus L, Brodersen P and Mims C A 2007 *J. Mater. Chem.* **17** 2500–5
[6] Strandbakke R, Cherepanov V A, Zuev A Y, Tsvetkov D S, Argirusis C, Sourkouni G, Prünte S and Norby T 2015 *Solid State Ion.* **278** 120–32
[7] Szpunar I *et al* 2020 *Materials* **13** 1–18
[8] Szpunar I *et al* 2020 *J. Am. Ceram. Soc.* **103** 1809–18
[9] Tang W, Ding H, Bian W, Wu W, Li W, Liu X, Gomez J Y, Regalado Vera C Y, Zhou M and Ding D 2020 *J. Mater. Chem.* A **8** 14600–8
[10] Kim J H, Yoo S, Murphy R, Chen Y, Ding Y, Pei K, Zhao B, Kim G, Choi Y and Liu M 2021 *Energy Environ. Sci.* **14** 1506–16
[11] Rioja-Monllor L, Bernuy-Lopez C, Fontaine M-L, Grande T and Einarsrud M-A 2019 *J. Mater. Chem.* A **7** 8609–19
[12] Wachowski S L *et al* 2020 *Acta Mater.* **199** 297–310
[13] Niu Y *et al* 2022 *Adv Energy Mater.* **12** 1–9
[14] Zhao C, Li Y, Zhang W, Zheng Y, Lou X, Yu B, Chen J, Chen Y, Liu M and Wang J 2020 *Energy Environ. Sci.* **13** 53–85
[15] Chen Y *et al* 2019 *ACS Catal.* **9** 7137–42
[16] Kousi K, Tang C, Metcalfe I S and Neagu D 2021 *Small* **17** 2006479
[17] López-García A, Almar L, Escolástico S, Hungría A B, Carrillo A J and Serra J M 2022 *ACS Appl. Energy Mater.* **5** 13269–83
[18] Irvine J T S, Neagu D, Verbraeken M C, Chatzichristodoulou C, Graves C and Mogensen M B 2016 *Nat. Energy* **1** 15014
[19] Myung J, Neagu D, Miller D N and Irvine J T S 2016 *Nature* **537** 528–31
[20] Neagu D *et al* 2023 *J. Phys. Energy* **5** 031501
[21] Carrillo A J, López-García A, Delgado-Galicia B and Serra J M 2024 *Chem. Commun.* **60** 7987–8007
[22] Tsvetkov D S, Ivanov I L, Malyshkin D A and Zuev A Y 2016 *J. Mater. Chem.* A **4** 1962–9
[23] Malyshkin D, Novikov A, Ivanov I, Sereda V, Tsvetkov D and Zuev A 2020 *J. Alloys Compd.* **845** 156309
[24] Tang C, Kousi K, Neagu D and Metcalfe I S 2021 *Chemistry* **27** 6666–75
[25] Balcerzak D *et al* 2023 *CrystEngComm* **25** 4306–16
[26] Park K *et al* 2024 *Energy Environ. Sci.* **17** 1175–88
[27] Spring J, Sediva E, Hood Z D, Gonzalez-Rosillo J C, O'Leary W, Kim K J, Carrillo A J and Rupp J L M 2020 *Small* **16** 2003224
[28] Neagu D, Tsekouras G, Miller D N, Menard H and Irvine J T 2013 *Nat. Chem.* **5** 916–23
[29] Carrillo A J and Serra J M 2021 *Catalysts* **11** 741
[30] Kim K J *et al* 2019 *J. Am. Chem. Soc.* **141** 7509–17
[31] Dong F, Ni M, Chen Y, Chen D, Tadé M O and Shao Z 2014 *J. Mater. Chem.* A **2** 20520–9
[32] Rudolph B, Tsiotsias A I, Ehrhardt B, Dolcet P, Gross S, Haas S, Charisou N D, Goula M A and Mascotto S 2023 *Adv. Sci.* **10** 1–12
[33] López-García A, Domínguez-Saldaña A, Carrillo A J, Navarrete L, Valls M I, García-Baños B, Plaza-Gonzalez P J, Catala-Civera J M and Serra J M 2023 *ACS Nano* **17** 23955–64
[34] Rietveld H M 1969 *J. Appl. Crystallogr.* **2** 65–71
[35] Kroumova E, Aroyo M I, Perez-Mato J M, Kirov A, Capillas C, Ivantchev S and Wondratschek H 2003 *Phase Transit.* **76** 155–70
[36] Schneider C A, Rasband W S and Eliceiri K W 2012 *Nat. Methods* **9** 671–5
[37] Haas S, Sun X, Conceição A L C, Horbach J and Pfeffer S 2023 *J. Synchrotron Radiat.* **30** 1156–67
[38] Kostorz G and Lovesey S W 1979 pp 1–67
[39] Breßler I, Kohlbrecher J and Thünemann A F 2015 *J. Appl. Crystallogr.* **48** 1587–98
[40] Rodríguez-Carvajal J 1993 *Physica* B **192** 55–69
[41] Pang S, Jiang X, Li X, Wang Q and Su Z 2012 *J. Power Sources* **204** 53–59
[42] Carrillo A J, Moya J, Bayón A, Jana P, de la Peña O'shea V A, Romero M, Gonzalez-Aguilar J, Serrano D P, Pizarro P and Coronado J M 2014 *Sol. Energy Mater. Sol. Cells* **123** 47–57
[43] Carrillo A J, Kim K J, Hood Z D, Bork A H and Rupp J L M 2020 *ACS Appl. Energy Mater.* **3** 1–34
[44] Wang J *et al* 2021 *Chem. Mater* **33** 5021–34
[45] Neagu D, Oh T-S, Miller D N, Menard H, Bukhari S M, Gamble S R, Gorte R J, Vohs J M and Irvine J T S 2015 *Nat. Commun.* **6** 8120
[46] Jennings D, Ricote S, Santiso J, Caicedo J and Reimanis I 2022 *Acta Mater.* **228** 117752
[47] Weber M L *et al* 2023 *J. Phys. Energy* **5** 014002
[48] Weber M L, Wilhelm M, Jin L, Breuer U, Dittmann R, Waser R, Guillon O, Lenser C and Gunkel F 2021 *ACS Nano* **15** 4546–60
[49] Kim Y H, Kang Y, Jo S, Jeong H, Neagu D and Myung J 2022 *Chem. Eng. J.* **441** 136025
[50] Neagu D *et al* 2019 *ACS Nano* **13** 12996–3005
[51] Cao X *et al* 2022 *Chem. Mater.* **34** 10484–94
[52] Kaabar W, Bott S and Devonshire R 2011 *Spectrochim. Acta* A **78** 136–41

[53] Hadjiev V G, Iliev M N and Vergilov I V 1988 *J. Phys. C: Solid State Phys.* **21** L199–L201
[54] Deng S, Chen N, Deng D, Li Y, Xing X and Wang Y 2015 *Ceram. Int.* **41** 11004–12
[55] Lorite I, Romero J J and Fernández J F 2012 *J. Raman Spectrosc.* **43** 1443–8
[56] Milt V G, Ulla M A and Miró E E 2005 *Appl. Catal.* B **57** 13–21
[57] Li T, Senesi A J and Lee B 2016 *Chem. Rev.* **116** 11128–80
[58] Neagu D *et al* 2017 *Nat. Commun.* **8** 1855
[59] Jennings D, Ricote S, Santiso J and Reimanis I 2020 *Scr. Mater.* **186** 401–5
[60] Vøllestad E, Schrade M, Segalini J, Strandbakke R and Norby T 2017 *J. Mater. Chem.* A **5** 15743–51
[61] Wang M, Papaioannou E I, Metcalfe I S, Naden A, Savaniu C D and Irvine J T S 2023 *Adv. Funct. Mater.* **33** 1–12